

Geophysical Research Letters®

RESEARCH LETTER

10.1029/2021GL096832

Key Points:

- Tectonic activity occurred during 65.6–59 Ma in East Asia and strengthened during 55–54 Ma in response to the India-Eurasia collision
- In East Asia, global warming led to enhanced weathering during 59–55 Ma and aridification during 54–50.5 Ma
- Global cooling between 50.5 and 37.6 Ma increased westerlies-derived moisture and enhanced chemical weathering in East Asia

Supporting Information:

Supporting Information may be found in the online version of this article.

Correspondence to:

H. Jiang,
hcjiang@ies.ac.cn;
hanchaojiang@hotmail.com

Citation:

Jiang, H., Zhang, J., Zhang, S., Zhong, N., Wan, S., Alsop, G. I., et al. (2022). Tectonic and climatic impacts on environmental evolution in East Asia during the Palaeogene. *Geophysical Research Letters*, 49, e2021GL096832. <https://doi.org/10.1029/2021GL096832>

Received 2 NOV 2021





Accepted 7 JAN 2022

Author Contributions:

Conceptualization: H. Jiang
Data curation: H. Jiang, S. Zhang, N. Zhong, S. Wan
Formal analysis: H. Jiang, N. Zhong
Funding acquisition: H. Jiang
Investigation: H. Jiang, J. Zhang, S. Zhang, N. Zhong, S. Wan, G. I. Alsop, H. Xu, Q. Guo, Z. Yan
Methodology: H. Jiang, S. Zhang, N. Zhong, H. Xu, Q. Guo
Project Administration: H. Jiang
Resources: S. Zhang, N. Zhong
Supervision: H. Jiang, J. Zhang, S. Wan, G. I. Alsop, Z. Yan
Validation: H. Jiang
Visualization: H. Xu, Q. Guo
Writing – original draft: H. Jiang
Writing – review & editing: H. Jiang, J. Zhang, G. I. Alsop, Z. Yan

© 2022. American Geophysical Union.
All Rights Reserved.

Tectonic and Climatic Impacts on Environmental Evolution in East Asia During the Palaeogene

H. Jiang¹ , J. Zhang¹, S. Zhang^{1,2}, N. Zhong¹, S. Wan³ , G. I. Alsop⁴ , H. Xu¹, Q. Guo^{1,2}, and Z. Yan⁵ 

¹State Key Laboratory of Earthquake Dynamics, Institute of Geology, China Earthquake Administration, Beijing, China, ²College of Earth Sciences, University of Chinese Academy of Sciences, Beijing, China, ³Key Laboratory of Marine Geology and Environment, Institute of Oceanology, Chinese Academy of Sciences, Qingdao, China, ⁴Department of Geology and Geophysics, School of Geosciences, University of Aberdeen, Aberdeen, UK, ⁵Institute of Geology, Chinese Academy of Geological Sciences, Beijing, China

Abstract Palaeogene environmental evolution in East Asia remains ambiguous. Here we present integrative work including magnetostratigraphy, grain-size, geochemistry, and clay mineralogy from a 1609 m-thick fluviolacustrine sequence in eastern China. The results reveal two periods of tectonic control alternating with three periods of climatic control on the sedimentary evolution. Tectonic activity in the study area, as revealed by particle coarsening and reduced weathering, occurred during 65.6–59 Ma and strengthened in Asia during 55–54 Ma in response to the India-Eurasia collision. Weathering gradually enhanced in East Asia during 59–55 Ma, probably caused by global warming. Continuous global warming during 54–50.5 Ma is responsible for enhanced aridification in East Asia. From 50.5 to 37.6 Ma, global cooling weakened evapotranspiration and increased westerlies-derived moisture. Both aspects increased effective moisture and chemical weathering in East Asia. These results shed light on how alternating tectonism and climate change impacted environmental evolution in Asia during the Palaeogene.

Plain Language Summary Most investigations in sedimentary basins generally focus exclusively on climatic signals at the expense of tectonic inputs. In this study, we extract both climatic and tectonic signals from long fluviolacustrine sediment records in eastern China comprehensively and objectively. We find that environmental evolution during the Paleogene of East Asia was dominated by tectonism during 65.6–59 and 55–54 Ma, and by climatic changes during 59–55 and 54–37.6 Ma. This work not only constrains the India-Asia collision to a short 55–54 Ma interval for the first time, but also offers a sound explanation for one of the most important but disputed issues of eolian sediments in the North Pacific Ocean.

1. Introduction

It has previously been established that tectonic activity influences the evolution of fluviolacustrine sedimentary sequences by affecting the provenance supply, while climate change modifies the sedimentary record through weathering and denudation (Najman, 2006). During the Early Cenozoic, many rifted basins developed in eastern China, while an array of compressional basins formed in western China, mostly due to the India-Eurasia collision and continued convergence (Yin & Harrison, 2000) and/or subduction of the western Pacific Plate (Northrup et al., 1995). Most of these basins are filled with non-marine sediments (Ye et al., 1993) and the documented signals suggest that the environmental evolution has been driven mainly by tectonic activity and/or climate change (Ye et al., 1993).

The Qinling-Qilian-Kunlun orogenic system (QQKOS) extends for ~3,000 km from east to west and formed in response to late Mid-Proterozoic to Cenozoic tectonism (Meng & Zhang, 2000; Peltzer et al., 1985). The QQKOS represents an important tectonic zone in Asia linking the India-Eurasia collision with extensive deformation in eastern China (Meng & Zhang, 2000; Peltzer et al., 1985; Figure 1). Field observations show that the faults of the QQKOS are still active today and may have undergone several tens of kilometers of post-Eocene left-lateral displacement (Peltzer et al., 1985). However, the impact of the India-Eurasia collision on eastern China during the Palaeogene, which represents the critical period of the India-Eurasia collision, has not been determined. On the other hand, a broad belt of aridity stretched across China from west to east during the Palaeogene (X. Sun and Wang, 2005), overlapping spatially with the QQKOS, with only the southern-most and northeastern China being

dominated by more humid conditions (X. Sun and Wang, 2005; Figure 1b). Under this overall dry environment, voluminous windblown deposits developed widely in fault-bounded basins of varying scales around the QQQOS during the Palaeogene (Jiang et al., 2014; Meng & Zhang, 2000). Exploring such a long terrestrial sedimentary sequence as preserved in the Paleogene of East Asia can help elucidate the terrestrial responses to both greenhouse climate change and to tectonism like the India-Eurasia collision (Gao et al., 2021).

In this study, we present a 1609 m-thick Paleocene-Eocene fluviolacustrine sedimentary sequence at Xijiadian (XJD) town (32°46'N, 111°12'E) in the Nanyang Basin of the eastern QQQOS (Figure 1). This stratigraphic record enables us to distinguish the relative roles of tectonic drivers and climatic drivers in the environmental evolution of East Asia during the Palaeogene. It is of profound scientific significance for signature extraction of climate change and tectonism from the long lacustrine sequences around the globe during this geologic period.

2. Geographic and Geological Setting

The studied section lies in the western Nanyang Basin, situated in the eastern QQQOS between the North and the South China blocks (Figure 1). Faults, hydrology, and lithology in the study area are generally distributed along the WNW-ESE and NEN-SWS directions (Jiang et al., 2014). In the north, mainly Cambrian (limestone and shale) and middle Sinian (dolomitized limestone, silicic limestone, and sandstone interbedded with limestones) strata occur. The middle part of the study area is comprised of the Eocene Dacangfang Formation, which is dominated by reddish mudstone, silty mudstone, muddy siltstone, sandy conglomerate, and conglomerate. In the south, the well-exposed Wudang quartz-sericite schist is interbedded with metasandstone and biotite-albite schist (Jiang et al., 2014).

Eastern China is currently influenced by the East Asian Summer Monsoon rainfall and is well vegetated. Therefore, long sedimentary sequences exposed in the eastern QQQOS (Figure 1) offer the rare chance to reconstruct the evolutionary history of a sedimentary environment driven by tectonic activity and climate change in East Asia.

3. Methods

Paleomagnetic samples were drilled and oriented by compass. The average sampling interval was 0.8 m. Paleomagnetic specimens were analyzed at the Paleomagnetism and Environmental Magnetism Laboratory in the Key Laboratory of Western China's Environmental System in Lanzhou University using the same demagnetizing and measuring procedures as Jiang et al. (2014).

In addition to the 4,279 samples for the Eocene strata (Jiang et al., 2014), a total of 1,598 samples were collected from the Paleocene sediments of the XJD section for grain-size analysis at a stratigraphic sampling interval of 0.09–1.28 m with a mean of 0.26 m. Organic material and carbonate were removed sequentially in grain size analysis. The samples were then analyzed using a Mastersizer 3000 laser grain-size analyzer at the State Key Laboratory of Earthquake Dynamics, Institute of Geology, China Earthquake Administration.

Major and trace elemental concentrations were determined at the Analytical Laboratory of Beijing Research Institute of Uranium Geology using a Philips PW2404 X-ray Fluorescence Spectrometer and a Finnigan MAT HR-ICP-MS (Element I) instrument, respectively. Clay mineral and Sr-Nd isotope analysis were carried out on the <2 μm fraction, which was separated using the Stokes' settling velocity principle, after the removal of carbonate and organic matter. Clay minerals were identified by X-ray diffraction using a D8 ADVANCE diffractometer with CuK (α) radiation (40 kV, 40 mA) in the Laboratory of the Institute of Oceanology, Chinese Academy of Sciences.

4. Results

4.1. Chronology of the XJD Sequence

This new magnetostratigraphic work focuses on the 420 m-thick Paleocene sequence of the XJD section with 525 samples. Five normal (N_1 – N_5) and five reversed (R_1 – R_5) magnetic polarity zones are observed (Figures S2–S4 in Supporting Information S1). Together with previous work on the Eocene strata and the constraints of a mammalian fossil *Rhombomylus* cf. *turpanensis* of the late Early Eocene at the Qingtangling site (~981 m at depth; Jiang

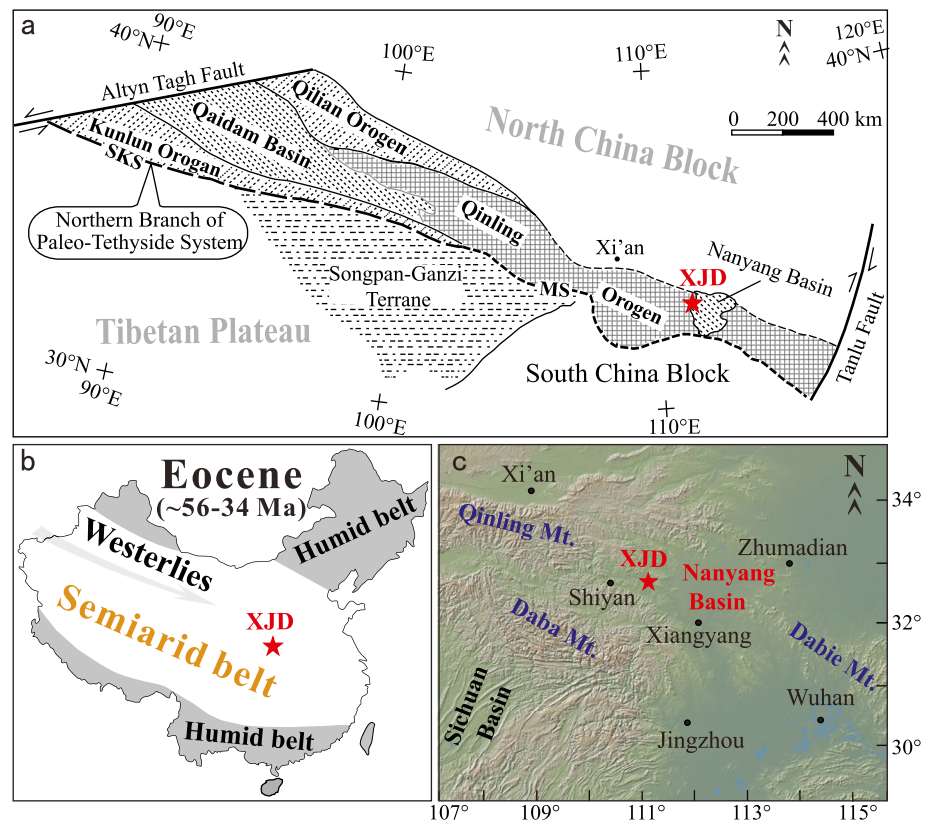


Figure 1. (a) Diagram showing the genetic linkage between the Qinling and adjacent orogens to the west (Meng & Zhang, 2000). (b) Distribution of semiarid belt and location of the Nanyang Basin (X. Sun & Wang, 2005). (c) Topography around the Nanyang Basin (<http://www.geomapapp.org/>). Note that the Mianlue suture is connected to the Southern Kunlun suture, and the South Qinling and Kunlun orogens together represent a northern branch of the Palaeo-Tethyan orogenic system (Meng & Zhang, 2000). XJD refers to the Xijiadian section. Red star marks the location of the study area.

et al., 2014), the XJD magnetic polarity column unambiguously and reliably correlates with the geomagnetic polarity timescale (Ogg, 2012; Figure S5 in Supporting Information S1), suggesting that the XJD sequence is continuous and spans from 65. to 37.6 Ma.

4.2. Provenance of the XJD Fine-Grained Sediments

A total of 5,877 grain-size samples are analyzed with a mean sampling interval of 0.27 m (equivalent to 4.76 ka). Systematic grain-size analysis shows that the median grain size (M_d) varies between 5.0 and 69.9 μm , with a mean of 22.6 μm (Figure 2a). The Sahu Y value, determined by the mean grain size, standard deviation, skewness, and kurtosis, is normally used to recognize an aeolian environment (Sahu, 1964; Note 1 in Supporting Information S1). The Y values of all samples range from -30.3 to -13.7 , lower than the threshold value of -2.74 (Figure 2b), supporting their windblown origin (Jiang et al., 2014). Furthermore, major and trace element compositions are often used to trace the provenance of dust deposits (Ding et al., 2001; Ferrat et al., 2011; Jahn et al., 2001). The major and trace element abundances of 136 XJD fluviolacustrine fine samples, which are evenly distributed through the entire sequence, show an exponential linear relationship with those of the loess-soil units from the Chinese Loess Plateau (CLP; Ding et al., 2001; Figure S9 in Supporting Information S1), further corroborating their windblown origin.

The $^{143}\text{Nd}/^{144}\text{Nd}$ ratios of 10 analyzed XJD samples display a restricted range of $-11.6 \sim -9.7$ (mean $\epsilon_{\text{Nd}} \approx -10.65 \pm 0.95$; Note 2 in Supporting Information S1), indicating a relatively young and uniform upper crustal source for the XJD fine-grained sediments (Jahn et al., 2001). This is consistent with the typical upper crustal patterns revealed by $(\text{La}/\text{Yb})_{\text{N}}$ (3.8–14.4, mean 10.4) and Eu/Eu^* (0.56–0.76, mean 0.64) from the XJD sequence, which are typical of dust particles of loess-soil units from the CLP (Jahn et al., 2001).

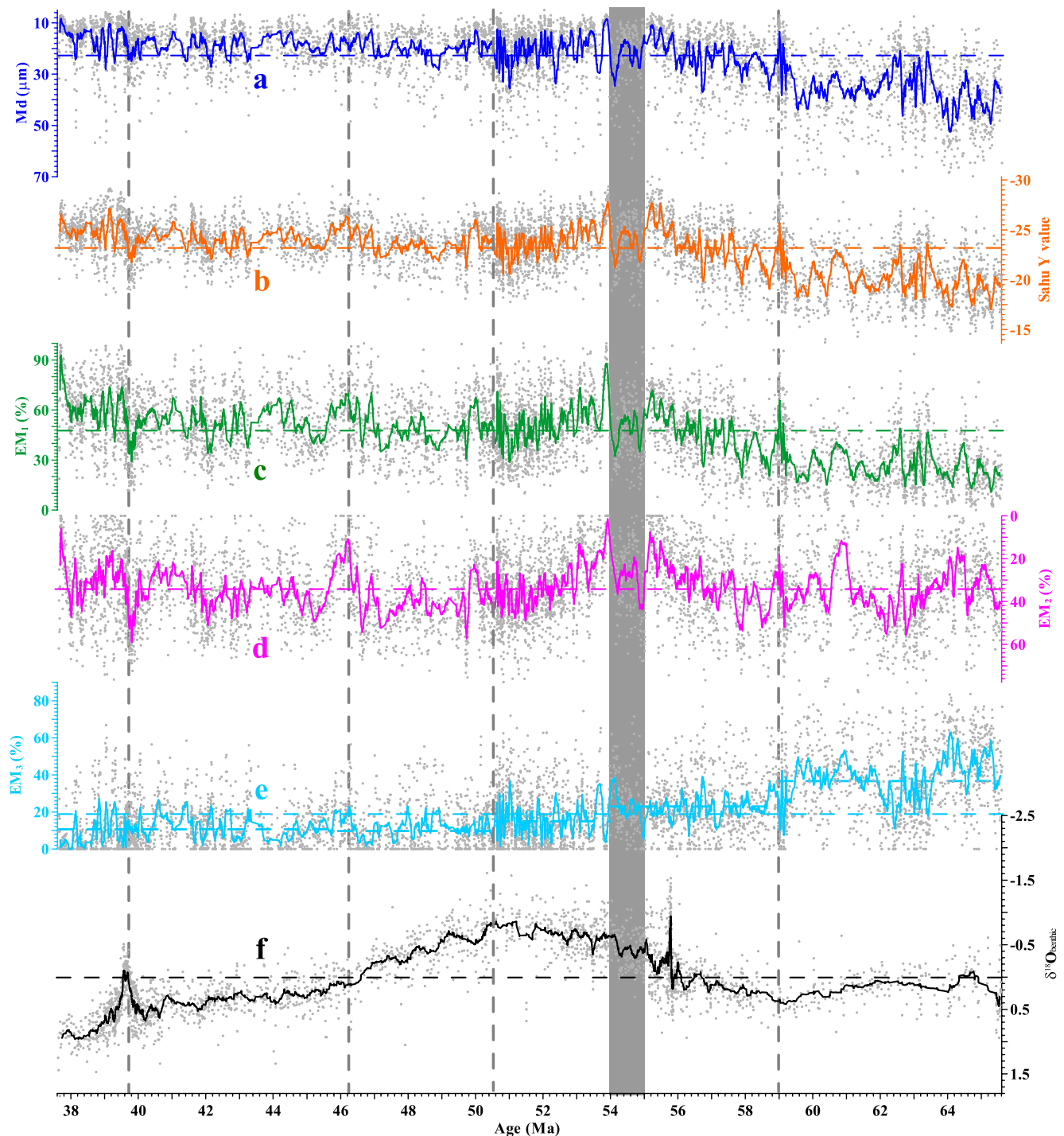


Figure 2. (a) The median grain-size, (b) Sahu Y value, and (c–e) three grain-size end-member abundances of the Xijiadian sequence in Hubei Province (eastern China) spanning 65.6–37.6 Ma plotted against paleomagnetic ages and their correlation with the (f) benthic $\delta^{18}\text{O}$ record (Cramer et al., 2009). The Sahu Y value less than -2.74 indicates an aeolian environment (Sahu, 1964) (Note 1 in Supporting Information S1). The gray dots define sample or data points. The solid lines represent a moving average with a window width of 21 points to detect their trends. The horizontal dashed lines indicate the average values of the records. The vertical dashed lines indicate the important shifts discussed in the text.

4.3. Variations in the XJD Grain-Size Record

Numerical unmixing of grain-size distribution data into constituent components, known as end-member analysis (EMA), can yield valuable information on geological processes (Jiang et al., 2017; Paterson & Heslop, 2015;

Weltje, 1997). The multiple correlation coefficient (R^2) and angle deviation are commonly used to determine goodness-of-fit (Paterson & Heslop, 2015), and one important principle is to explain the observed compositional variation with a minimum number of end members (Weltje, 1997). The grain size of all 5,877 samples is mainly concentrated in the range of 0–100 μm with a unimodal distribution (Figure S8a in Supporting Information S1). To approximate the observed compositional variation, one to five end members are modeled by EMA in this study. The correlation maps for R^2 and angle deviation with number of end members suggest that end-member modeling improves greatly from two to three end members, but improves less from three to four end members (Figures S8b and S8c in Supporting Information S1). Accordingly, three end-members are the minimum number that are the closest to the truth (Figure S7 in Supporting Information S1), and they include EM_1 (0.3–243.0 μm , peak at 6.9 μm), EM_2 (0.5–306.6 μm , peak at 29.5 μm), and EM_3 (0.7–546.6 μm , peak at 78.1 μm ; Figure S8 in Supporting Information S1). EM_1 (0%–100%, mean 47.2%) can be transported through long-term suspension, whereas EM_2 (0%–77.8%, mean 34.1%), and EM_3 (0%–90.6%, mean 18.7%; Figures 2c–2e) represent regional and local windblown sediments, respectively (Jiang et al., 2014; Pye, 1987).

We averaged three end-members with a window width of 21 points to detect their varying trends. There are two patterns: dramatic changes and steady evolution. The grain-size record from 65.6 to 59 Ma has the strongest fluctuations with the largest amplitude (7.2–69.9 μm) and the maximum Md of the sequence (mean 34.8 μm). The local windblown fraction (EM_3) reaches 90.6%, with the highest mean of 36.8% during 65.6–59 Ma. The dust particles become coarse at 55–54 Ma, with an abrupt increase in EM_2 and a corresponding decrease in EM_1 , similar to a 1 Myr-duration wedge (Figures 2c and 2d). In contrast, the other periods display a relatively steady evolution; specifically, the dust particles gradually fine from 59 to 55 Ma, coarsen from 54 to 50.5 Ma, and slowly fine again from 50.5 to 37.6 Ma (Figure 2).

4.4. Major and Trace Element Variations

The addition of fresh material to sedimentary basins commonly results in a decrease in the immobile element content and an increase in the mobile element content, whereas stepwise weathering and leaching usually induce the opposite change.

During 65.6–59 Ma, the content of immobile TiO_2 (0.5%–0.9%) has the lowest mean (0.6%) of the sequence with unstable oscillations (Figure 3a). It steadily increases from 59 to 55 Ma, decreases significantly during 55–54 Ma, and decreases from 54 to 37.6 Ma but remains above the overall average. The abundance of mobile Na_2O (0.5%–3.52%) and the molar ratios of $\text{Na}_2\text{O}/\text{Al}_2\text{O}_3$ (0.03–0.49) during 65.6–55 Ma are the most scattered but their average values (2.05% and 0.24%) are the highest of the whole sequence, which then exhibits a decreasing trend from 59 to 55 Ma (Figure 3b). They increase significantly during 55–54 Ma and oscillate generally below the average values after 54 Ma. The other major elements and 17 trace elements all have distinct changes at 55–54 Ma (Figures S10 and S11 and Note 4 in Supporting Information S1). Noticeably, the ratios of $Y/\Sigma\text{REE}$, $Y/\text{Nd}_{\text{PAAS}}$, $(\text{Eu}/\text{Eu}^*)_{\text{PAAS}}$, and $(\text{La}/\text{Er})_{\text{PAAS}}$ normalized to post-Archean Australian shale (PAAS) and are utilized to identify provenance changes independent of particle size (Ferrat et al., 2011). At 55–54 Ma, the first three ratios increase dramatically (Figures S12a–S12c in Supporting Information S1), whereas the last ratio decreases significantly (Figure S12d in Supporting Information S1). They are followed by the opposite trends for these four ratios after ~54 Ma.

The chemical index of alteration (CIA) is generally used as an indicator of the degree of weathering of sediments (Note 5 in Supporting Information S1). The CIA values (55.3–75.7) of the analyzed samples have an overall low average of 67.2 (Figure 3c), indicating deposition under a dry and weak-weathering environment. During 65.6–59 Ma, the CIA values fluctuate strongly between 55.3 and 72.3, with a mean value of 63.0. The CIA values increase from 59 to 55 Ma (mean 66.1) and decrease abruptly at 55–54 Ma with the lowest average value of 60.8 for the whole sequence. After 54 Ma, the CIA values show small oscillations, with most samples above the average (67.2; Figure 3c).

4.5. Clay Minerals and Their Sr-Nd Isotopic Variations

The clay mineral assemblages of the XJD sequence are dominated by smectite (6%–91%, mean 36%), illite (7%–60%, mean 34%), and palygorskite (0%–59%, mean 25%), with minor amounts of chlorite (0%–9%, mean 2%) and kaolinite (0%–7%, mean 2%; Figures 3d–3f, Figure S14 and Table S2 in Supporting Information S1). During

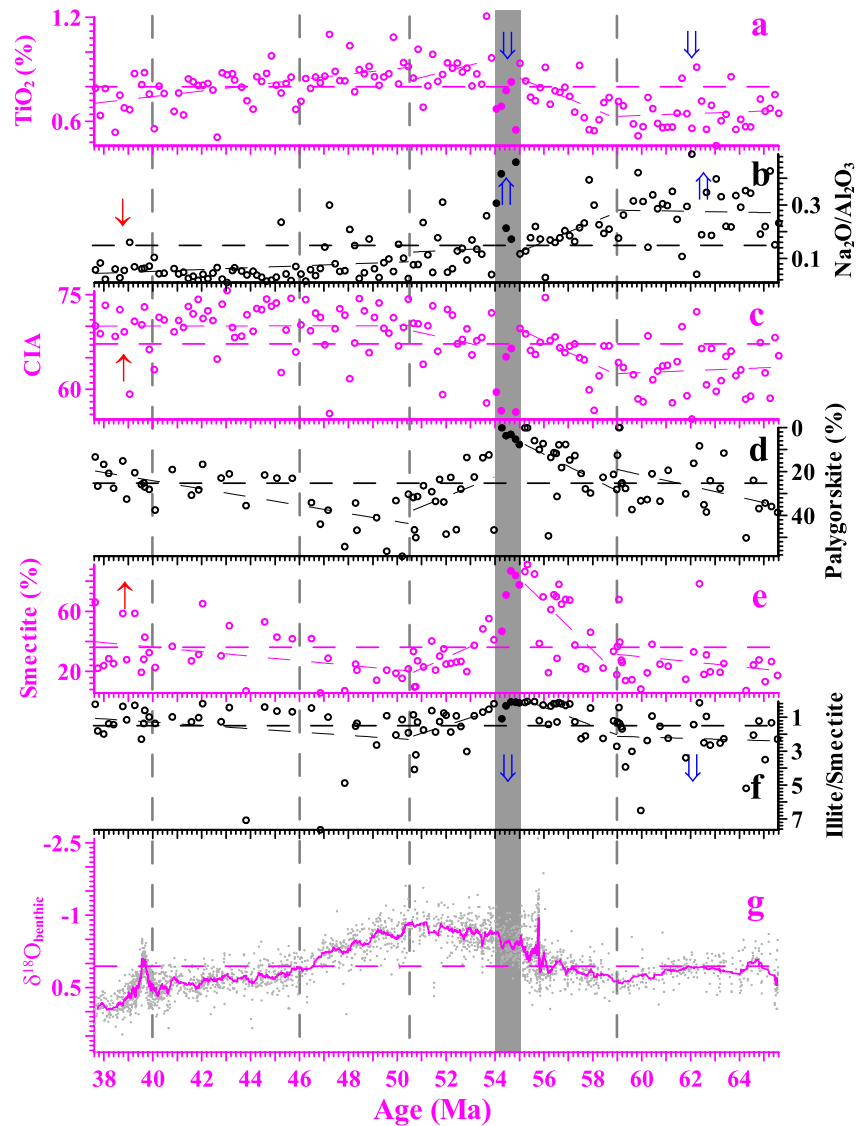


Figure 3. Comparison of varying values of (a) TiO_2 , (b) $\text{Na}_2\text{O}/\text{Al}_2\text{O}_3$ (molar ratio), (c) chemical index of alteration, (d) palygorskite, (e) smectite, (f) and illite/smectite in fluviolacustrine sediments from the Xijiadian sequence in Hubei Province (eastern China) with variations in the (g) benthic $\delta^{18}\text{O}$ record (Cramer et al., 2009). The gray points and open circles represent sample or data points. The dashed horizontal or oblique lines indicate the average or fitting trends. The vertical dashed lines and the gray band indicate the time points and intervals discussed in the text. The red single-line arrows indicate the variation of weathering while the blue double-line arrows indicate the variation in fresh material sources with upward arrows showing the trend of increase and vice versa.

65.6–59 Ma, the content of illite (12%–58%, mean 43%) and the ratio of illite/smectite (0.15–6.50, mean 2.24) are not only the highest but also the most scattered of the sequence, while most smectite values are lower than the average (Figures 3e and 3f). Palygorskite shows extremely scattered values (Figure 3d). From 59 to 55 Ma, content variation of these major clay minerals become stable, with decrease in illite and palygorskite and increase in smectite (Figures 3d–3f). At 55–54 Ma, illite and the illite/smectite ratio increase rapidly, smectite decreases significantly, and palygorskite remains the lowest of the sequence. From 54 to 50.5 Ma, smectite decreases and palygorskite and the illite/smectite ratio increase, while these three proxies show the opposite trend from 50.5 to 37.6 Ma.

A strong inverse relationship between smectite and palygorskite reveals the authigenic transformation of palygorskite from smectite (Figures 3d and 3e, Figure S16a in Supporting Information S1). Furthermore, a stronger

inverse relationship between illite and the sum of palygorskite and smectite (Figure S16b in Supporting Information S1) suggests that the illite in the study area has been transformed into palygorskite and smectite. Clay components of the XJD fluviolacustrine sediments have Sr-Nd isotopic features similar to those from the northern margin of the TP instead of those from the eastern QKOS (Note 2 in Supporting Information S1). This implies that they are mainly transported by wind from the northern margin of the TP.

5. Discussion and Implications

Some layers of sandstone and sandy conglomerate are occasionally developed in the XJD section, reflecting the fluvial contribution in the Nanyang Basin (Jiang et al., 2014). This basin is located in the piedmont area of the East Qinling Mountains (Figure 1c). The floodplains may provide silt particles for the Nanyang Basin similar to those from the western Qinling Mountains for the Tianshui Basin (S. Liu et al., 2019). However, there is no evidence in the field of hydrodynamic waxing or waning expressed as upward coarsening or fining particles. Correspondingly, sedimentary structures such as cross-bedding and ripples related to current action were rarely observed in the XJD section. Instead, massive structure, a typical feature of dust deposition (Ding et al., 2001), commonly exists in the XJD section. Noticeably, fluvial sedimentation generally has a momentary process with a high-energy environment while dust deposition occurs over a long duration with the inherent characteristics of a low-energy environment. Accordingly, we focus on slow deposition of fine dust particles rather than fluvial deposits in this study.

5.1. Weathering Affected by Climate Change

From 59 to 55 Ma, the XJD dust particles consistently become finer (Figure 2). The immobile TiO_2 content, CIA, and smectite increase, while the mobile Na_2O content, the $\text{Na}_2\text{O}/\text{Al}_2\text{O}_3$ ratio, the illite/smectite ratio, and palygorskite proportion decrease (Figure 3). These trends are probably due to enhanced chemical weathering induced by global warming, as revealed by the benthic $\delta^{18}\text{O}$ record (Cramer et al., 2009; Figure 2f).

From 54 to 50.5 Ma, the local particle supply EM_3 decreases below the average, implying a tectonically stable environment (Figure 2e). However, the XJD dust particles become coarse (Figure 2a) as the regional particle supply EM_2 increases above the average (Figure 2d). In addition, illite content and CIA increase slightly, while the illite/smectite ratio and palygorskite (probably transformed from smectite) increase significantly (Figure 3). These results indicate a slight weathering-enhanced and high-alkalinity (Singer, 1980) sedimentary environment in the Nanyang Basin. This enhanced aridification (Jiang et al., 2014) is likely to result from sustained warming globally based on the benthic $\delta^{18}\text{O}$ record (Cramer et al., 2009; Figure 2f).

The period from 50.5 to 37.6 Ma is characterized by slow fining of the XJD dust particles, with the smallest mean Md (18.2 μm) and the lowest mean EM_3 proportion (10.6%) of the sequence. The generally high CIA values and TiO_2 contents and low contents of Na_2O and ratio of $\text{Na}_2\text{O}/\text{Al}_2\text{O}_3$ suggest a slightly increased weathering, though with a generally low intensity under an arid environment (Figures 3a–3c). The stepwise content decrease in palygorskite from 50.5 to 37.6 Ma indicates a decreased alkalinity and thus an increased humidity of the depositional environment (Figure 3d). The increase in smectite and the decrease in the illite/smectite ratio imply increased weathering in the study area, although illite remains relatively stable in content (Figures 3e and 3f). Here we propose that global cooling from 50.5 to 37.6 Ma weakened evapotranspiration, enhanced the westerly circulation (Jiang et al., 2014), and consequently increased moisture carried by the westerly wind (Gao et al., 2021). Both aspects increased effective moisture and consequently enhanced chemical weathering in East Asia. This interpretation is also supported by the positive response of the XJD sedimentation to two salient climatic events. The appearance of ice in the Arctic at ~ 46 Ma (Moran et al., 2006) indicates significant global cooling. The obvious response of the XJD sequence at ~ 46 Ma includes the fining of dust particles (Figure 2), high CIA values and smectite contents (Figures 3c and 3e), low $\text{Na}_2\text{O}/\text{Al}_2\text{O}_3$ and illite/smectite ratios, and reduced alkalinity as revealed by the decrease in palygorskite content (Figures 3b, 3d, and 3f). A global warming event at ~ 40 Ma related to a brief reversal of the long-term Eocene cooling trend (Bohatty & Zachos, 2003; Bohatty et al., 2009), induced the opposite responses to those at ~ 46 Ma (Figures 2 and 3b–3e). Hence, during the Palaeogene, East Asia was controlled by a planetary climate rather than a monsoon climate.

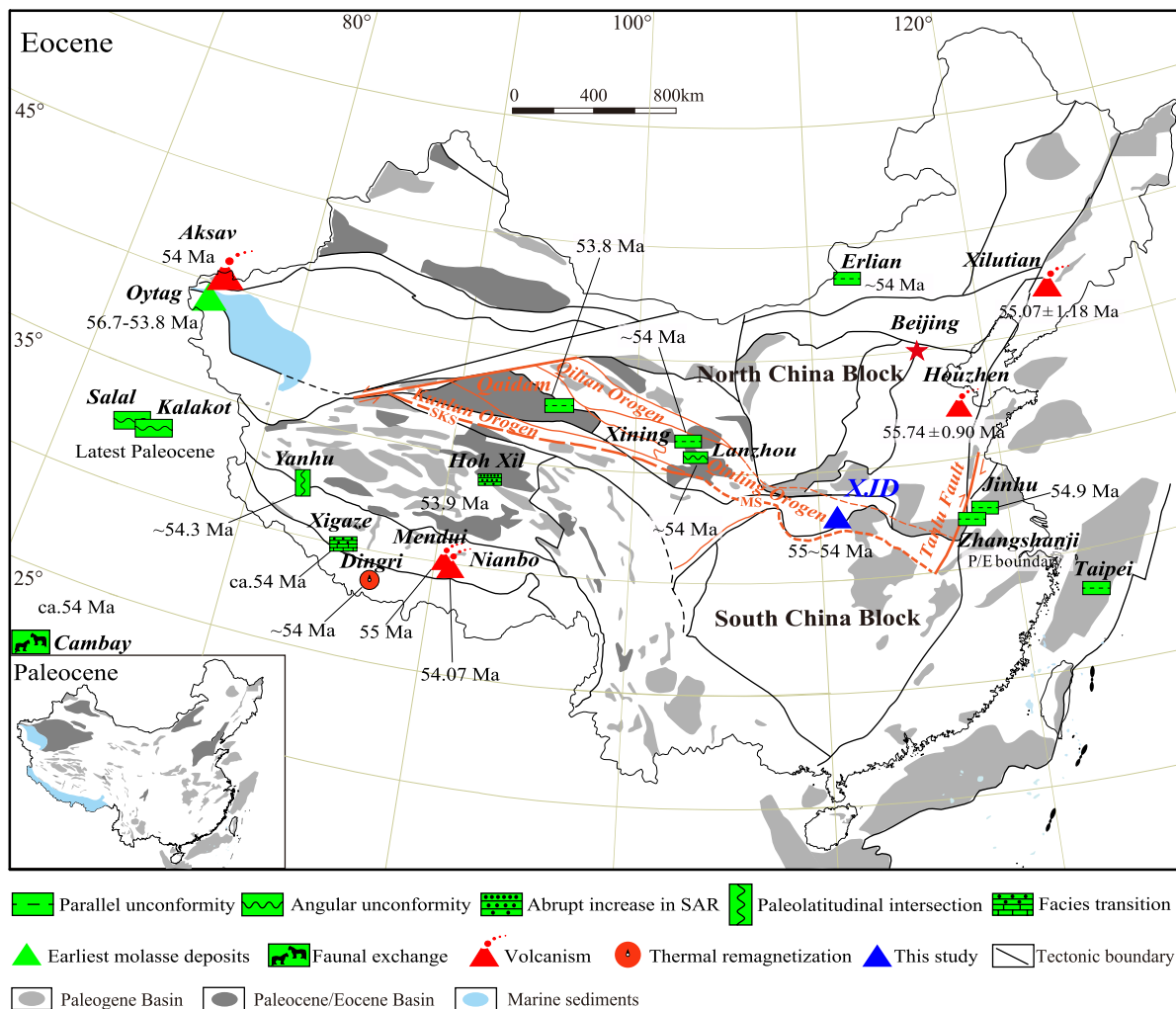


Figure 4. Diagram showing the consistent kinematic properties of the Qinling-Qilian-Kunlun orogenic system and locations with corroborating evidence of the strong tectonic activities at 55–54 Ma in Asia. These include stratigraphic unconformities, abrupt increases in the sediment accumulation rate, palaeolatitudinal intersection, facies transitions, molasse deposits, faunal exchange, volcanism, and thermal remagnetization (Table S3 in Supporting Information S1).

5.2. Enhanced Tectonic Activity at 55–54 Ma

The period of 65.6–59 Ma is characterized by the highest mean values and the strongest oscillations in the local dust supply (EM_3), the lowest average TiO_2 content, the highest average Na_2O/Al_2O_3 and illite/smectite ratios, and a low mean CIA (63.0) in the XJD sequence. Additionally, the period 55–54 Ma features pronounced increases in the regional dust supply (EM_2) and the Na_2O/Al_2O_3 and illite/smectite ratios, and significant decreases in the immobile TiO_2 content, CIA, and smectite. These features indicate the significant addition of fresh material into the XJD sediments and a resultant decrease in weathering. We ascribe these changes to tectonic activity around the eastern QQQOS during 65.6–59 Ma, and significantly strengthened tectonic activity in Asia during 55–54 Ma in response to the India-Eurasia collision at ~55 Ma as revealed by the Indian Ocean magnetic anomalies (Powell & Conaghan, 1975). In addition to the effects observed in our study area, the intense tectonic activity during 55–54 Ma produces a widespread disconformity (Fang et al., 2019; Singh, 2003; Y. Wang et al., 2010; Xue et al., 2013; Y. Zhang et al., 2014; Zheng et al., 1999; X. Zhou et al., 2019), the onset of India-Eurasia terrestrial faunal exchange (Clementz et al., 2011), an abrupt increase in sediment accumulation (Jin et al., 2018), facies transitions (Orme et al., 2015), palaeolatitudinal intersection (Ma et al., 2014), thermal remagnetization (Tong et al., 2008), the formation of many basins in Asia (J. Sun and Jiang, 2013), and the closure of the Neo-Tethys Ocean (J. Li et al., 2015; Figure 4, Note 6 and Table S3 in Supporting Information S1). Furthermore, the intense tectonic activity during 55–54 Ma also generates widespread magmatic eruptions in Asia (Bazhenov &

Mikolaichuk, 2002; Z. Chen et al., 2014; J. R. Li et al., 1989; Z. Sun et al., 2010; S. Zhou et al., 2004). These features for the first time collectively constrain the India-Eurasia collision to a short interval from 55 to 54 Ma, which is consistent with the timing of an almost complete halt to the northward motion of India (Sclater & Fisher, 1974), the end of suturing and the beginning of the so-called hard collision at ~55 Ma (Klootwijk et al., 1992).

5.3. Impact on the North Pacific Ocean

The eolian sediments in the North Pacific Ocean display sharp decreases in grain size from continuously coarse grained in the Paleocene to continuously fine grained in the Eocene, while the peak accumulation rate decreases by almost a factor of 3 across the Paleocene/Eocene boundary (Janecek & Rea, 1983; Rea, 1994). Both phenomena have for decades remained enigmatic due to the absence of systematic investigations into long continental sedimentary records. Based on our work, we propose that the occurrence of tectonic activity around the QQKOS during 65.6–59 Ma and its enhancement in Asia at 55–54 Ma in response to the India-Eurasia collision, are responsible for both phenomena. Strong earthquakes associated with tectonic activity can generate large amounts of dust particles in arid to semiarid regions (Jiang et al., 2017), which could have been transported to the basins around the QQKOS and even as far as the North Pacific Ocean during the Paleogene. In the Nanyang Basin, the dust particles are generally coarse during 65.6–55 Ma and remain mostly fine after 54 Ma (Figure 2), which contributes to our understanding of the patterns of aeolian sediments in the North Pacific Ocean (Janecek & Rea, 1983; Rea, 1994). This is the first study to develop a new source-to-sink model that links basin deposition during the Paleogene in Asia to pelagic sedimentation in the North Pacific Ocean in response to the India-Eurasia collision. Noticeably, the availability of dust particles in Asia, instead of transport capacity, plays the primary role in deposition of the aeolian sediments in the North Pacific Ocean from the Paleocene to the Eocene, given that the low thermal gradients and less vigorous atmospheric circulation during this period (Janecek & Rea, 1983; Suan et al., 2017) could have weakened the dynamics of dust transport.

Data Availability Statement

Source data are provided with this paper and are deposited in Mendeley (doi: 10.17632/gdppp4r97d.1).

Acknowledgments

This work is financially supported by the National Natural Science Foundation of China (41572346) and National Nonprofit Fundamental Research Grant of China, Institute of Geology, China Earthquake Administration (IGCEA1906). We feel grateful to Prof. Jin Meng, Prof. Peter D. Clift, and Dr. Jessica A. Thompson Jobe for the valuable comments and constructive suggestions. We thank Dr. Zuolin Chen and Ms Xue Mao for assistance in the field, and Ms Yanhao Li and Mr Youliang Bai for help in the laboratory. We appreciate Prof. Lucy Flesch (editor) for handling our manuscript and two anonymous reviewers for constructive reviews.

References

- Bazhenov, M. L., & Mikolaichuk, A. V. (2002). Paleomagnetism of Paleogene basalts from the Tien Shan, Kyrgyzstan: Rigid Eurasia and dipole geomagnetic field. *Earth and Planetary Science Letters*, 195(1–2), 155–166. [https://doi.org/10.1016/S0012-821X\(01\)00586-6](https://doi.org/10.1016/S0012-821X(01)00586-6)
- Bohaty, S. M., & Zachos, J. C. (2003). Significant Southern Ocean warming event in the late middle Eocene. *Geology*, 31(11), 1017–1020. <https://doi.org/10.1130/G19800.1>
- Bohaty, S. M., Zachos, J. C., Florindo, F., & Delaney, M. L. (2009). Coupled greenhouse warming and deep-sea acidification in the middle Eocene. *Paleoceanography*, 24, PA2207. <https://doi.org/10.1029/2008PA001676>
- Chen, Z., Ding, Z., Tang, Z., Wang, X., & Yang, S. (2014). Early Eocene carbon isotope excursions: Evidence from the terrestrial coal seam in the Fushun Basin, Northeast China. *Geophysical Research Letters*, 41(10), 3559–3564. <https://doi.org/10.1002/2014GL059808>
- Clementz, M., Bajpai, S., Ravikant, V., Thewissen, J. G. M., Saravanan, N., Singh, I. B., & Prasad, V. (2011). Early Eocene warming events and the timing of terrestrial faunal exchange between India and Asia. *Geology*, 39(1), 15–18. <https://doi.org/10.1130/G31585.1>
- Cramer, B. S., Toggweiler, J. R., Wright, J. D., Katz, M. E., & Miller, K. G. (2009). Ocean overturning since the Late Cretaceous: Inferences from a new benthic foraminiferal isotope compilation. *Paleoceanography*, 24, PA4216. <https://doi.org/10.1029/2008pa001683>
- Ding, Z., Sun, J., Yang, S., & Liu, T. (2001). Geochemistry of the Pliocene red clay formation in the Chinese Loess Plateau and implications for its origin, source provenance and paleoclimate change. *Geochimica et Cosmochimica Acta*, 65(6), 901–913. [https://doi.org/10.1016/S0016-7037\(00\)00571-8](https://doi.org/10.1016/S0016-7037(00)00571-8)
- Fang, X., Fang, Y., Zan, J., Zhang, W., Song, C., Appel, E., et al. (2019). Cenozoic magnetostratigraphy of the Xining Basin, NE Tibetan Plateau, and its constraints on paleontological, sedimentological and tectonomorphological evolution. *Earth-Science Reviews*, 190, 460–485. <https://doi.org/10.1016/j.earscirev.2019.01.021>
- Ferrat, M., Weiss, D. J., Strekopytov, S., Dong, S., Chen, H., Najorka, J., et al. (2011). Improved provenance tracing of Asian dust sources using rare earth elements and selected trace elements for palaeomonsoon studies on the eastern Tibetan Plateau. *Geochimica et Cosmochimica Acta*, 75(21), 6374–6399. <https://doi.org/10.1016/j.gca.2011.08.025>
- Gao, Y., Ibarra, D. E., Caves Rugenstein, J. K., Chen, J., Kukla, T., Methner, K., et al. (2021). Terrestrial climate in mid-latitude East Asia from the latest Cretaceous to the earliest Paleogene: A multiproxy record from the Songliao Basin in northeastern China. *Earth-Science Reviews*, 216, 103572. <https://doi.org/10.1016/j.earscirev.2021.103572>
- Jahn, B. M., Gallet, S., & Han, J. (2001). Geochemistry of the Xining, Xifeng and Jixian sections, Loess Plateau of China: Eolian dust provenance and paleosol evolution during the last 140 ka. *Chemical Geology*, 178(1–4), 71–94. [https://doi.org/10.1016/S0009-2541\(00\)00430-7](https://doi.org/10.1016/S0009-2541(00)00430-7)
- Janecek, T. R., & Rea, D. K. (1983). Eolian deposition in the northeast Pacific Ocean: Cenozoic history of atmospheric circulation. *The Geological Society of America Bulletin*, 94(6), 730–738. [https://doi.org/10.1130/0016-7606\(1983\)94<730:EDITNP>2.0.CO;2](https://doi.org/10.1130/0016-7606(1983)94<730:EDITNP>2.0.CO;2)
- Jiang, H., Zhong, N., Li, Y., Ma, X., Xu, H., Shi, W., et al. (2017). A continuous 13.3-ka record of seismogenic dust events in lacustrine sediments in the eastern Tibetan Plateau. *Scientific Reports*, 7, 15686. <https://doi.org/10.1038/s41598-017-16027-8>

- Jiang, H., Zhong, N., Li, Y., Xu, H., Ma, X., Meng, Y., & Mao, X. (2014). Magnetostratigraphy and grain size record of the Xijiadian fluvio-lacustrine sediments in East China and its implied stepwise enhancement of the westerly circulation during the Eocene period. *Journal of Geophysical Research: Solid Earth*, *119*(10), 7442–7457. <https://doi.org/10.1002/2014JB011225>
- Jin, C., Liu, Q., Liang, W., Roberts, A. P., Sun, J., Hu, P., et al. (2018). Magnetostratigraphy of the Fenghuoshan group in the Hoh Xil Basin and its tectonic implications for India–Eurasia collision and Tibetan Plateau deformation. *Earth and Planetary Science Letters*, *486*, 41–53. <https://doi.org/10.1016/j.epsl.2018.01.010>
- Klootwijk, C. T., Gee, J. S., Peirce, J. W., Smith, G. M., & McFadden, P. L. (1992). An early India-Asia contact: Paleomagnetic constraints from Ninetyeast Ridge, ODP Leg 121. *Geology*, *20*(5), 395–398. [https://doi.org/10.1130/0091-7613\(1992\)020<0395:AEIACP>2.3.CO;2](https://doi.org/10.1130/0091-7613(1992)020<0395:AEIACP>2.3.CO;2)
- Li, J., Hu, X., Garzanti, E., An, W., & Wang, J. (2015). Paleogene carbonate microfacies and sandstone provenance (Gamba area, South Tibet): Stratigraphic response to initial India–Asia continental collision. *Journal of Asian Earth Sciences*, *104*(May), 39–54. <https://doi.org/10.1016/j.jseas.2014.10.027>
- Li, J. R., Xu, J. L., Yao, Y. M., & Xiang, W. D. (1989). Paleocene Houzhen formation in Changwei, Shandong Province. *Chinese Science Bulletin*, *34*, 1882–1884.
- Liu, S., Li, J., Stockli, D. F., Song, C., Guo, B., Stockli, L. D., et al. (2019). Reappraisal of Miocene eolian deposition in Tianshui Basin, China, based on an investigation of stratigraphy and provenance. *The Geological Society of America Bulletin*, *131*(7–8), 1312–1332. <https://doi.org/10.1130/B32056.1>
- Ma, Y., Yang, T., Yang, Z., Zhang, S., Wu, H., Li, H., et al. (2014). Paleomagnetism and U-Pb zircon geochronology of Lower Cretaceous lava flows from the western Lhasa terrane: New constraints on the India-Asia collision process and intracontinental deformation within Asia. *Journal of Geophysical Research: Solid Earth*, *119*(10), 7404–7424. <https://doi.org/10.1002/2014JB011362>
- Meng, Q., & Zhang, G. (2000). Geologic framework and tectonic evolution of the Qinling orogen, central China. *Tectonophysics*, *323*(3–4), 183–196. [https://doi.org/10.1016/S0040-1951\(00\)00106-2](https://doi.org/10.1016/S0040-1951(00)00106-2)
- Moran, K., Backman, J., Brinkhuis, H., Clements, S. C., Cronin, T., Dickens, G. R., et al. (2006). The Cenozoic palaeoenvironment of the Arctic Ocean. *Nature*, *441*(7093), 601–605. <https://doi.org/10.1038/nature04800>
- Najman, Y. (2006). The detrital record of orogenesis: A review of approaches and techniques used in the Himalayan sedimentary basins. *Earth-Science Reviews*, *74*(1–2), 1–72. <https://doi.org/10.1016/j.earscirev.2005.04.004>
- Northrup, C. J., Royden, L. H., & Burchfiel, B. C. (1995). Motion of the Pacific plate relative to Eurasia and its potential relation to Cenozoic extension along the eastern margin of Eurasia. *Geology*, *23*(8), 719–722. [https://doi.org/10.1130/0091-7613\(1995\)023<0719:MOTPPR>2.3.CO;2](https://doi.org/10.1130/0091-7613(1995)023<0719:MOTPPR>2.3.CO;2)
- Ogg, J. G. (2012). In F. M. Gradstein, J. G. Ogg, M. D. Schmitz, & G. M. Ogg (Eds.), *The geologic time scale* (pp. 85–113). Elsevier.
- Orme, D. A., Carrapa, B., & Kapp, P. (2015). Sedimentology, provenance and geochronology of the upper Cretaceous–lower Eocene western Xigaze Forearc basin, southern Tibet. *Basin Research*, *27*(4), 387–411. <https://doi.org/10.1111/bre.12080>
- Paterson, G. A., & Heslop, D. (2015). New methods for unmixing sediment grain size data. *Geochemistry, Geophysics, Geosystems*, *16*(12), 4494–4506. <https://doi.org/10.1002/2015GC006070>
- Peltzer, G., Tapponnier, P., Zhitao, Z., & Qin, X. Z. (1985). Neogene and quaternary faulting in and along the Qinling Shan. *Nature*, *317*(6037), 500–505. <https://doi.org/10.1038/317500a0>
- Powell, C. M., & Conaghan, P. J. (1975). Tectonic models of the Tibetan plateau. *Geology*, *3*(12), 727–731. [https://doi.org/10.1130/0091-7613\(1975\)3<727:tmottp>2.0.co;2](https://doi.org/10.1130/0091-7613(1975)3<727:tmottp>2.0.co;2)
- Pye, K. (1987). *Eolian dust and dust deposits*. Academic Press.
- Rea, D. K. (1994). The paleoclimatic record provided by eolian deposition in the deep-sea: The geologic history of wind. *Reviews of Geophysics*, *35*, 159–195. <https://doi.org/10.1029/93rg03257>
- Sahu, B. K. (1964). Depositional mechanisms from the size analysis of clastic sediments. *Journal of Sedimentary Petrology*, *34*(1), 73–83. <https://doi.org/10.1306/74D70FCE-2B21-11D7-8648000102C1865D>
- Sclater, J. G., & Fisher, R. L. (1974). Evolution of the East: Central Indian Ocean, with emphasis on the tectonic setting of the Ninetyeast Ridge. *The Geological Society of America Bulletin*, *85*(5), 683–702. [https://doi.org/10.1130/0016-7606\(1974\)85<683:eoteci>2.0.co;2](https://doi.org/10.1130/0016-7606(1974)85<683:eoteci>2.0.co;2)
- Singer, A. (1980). The paleoclimatic interpretation of clay minerals in soils and weathering profiles. *Earth-Science Reviews*, *15*(4), 303–326. [https://doi.org/10.1016/0012-8252\(80\)90113-0](https://doi.org/10.1016/0012-8252(80)90113-0)
- Singh, B. P. (2003). Evidence of growth fault and forebulge in the Late Paleocene (57.9–54.7 Ma), western Himalayan foreland basin, India. *Earth and Planetary Science Letters*, *216*(4), 717–724. [https://doi.org/10.1016/S0012-821X\(03\)00540-5](https://doi.org/10.1016/S0012-821X(03)00540-5)
- Suan, G., Popescu, S. M., Suc, J. P., Schnyder, J., Fauquette, S., Baudin, F., et al. (2017). Subtropical climate conditions and mangrove growth in Arctic Siberia during the early Eocene. *Geology*, *45*(6), 539–542. <https://doi.org/10.1130/G38547.1>
- Sun, J., & Jiang, M. (2013). Eocene seawater retreat from the southwest Tarim Basin and implications for early Cenozoic tectonic evolution in the Pamir Plateau. *Tectonophysics*, *588*, 27–38. <https://doi.org/10.1016/j.tecto.2012.11.031>
- Sun, X., & Wang, P. (2005). How old is the Asian monsoon system? Paleobotanical records from China. *Palaeogeography, Palaeoclimatology, Palaeoecology*, *222*(3–4), 181–222. <https://doi.org/10.1016/j.palaeo.2005.03.005>
- Sun, Z., Jiang, W., Li, H., Pei, J., & Zhu, Z. (2010). New paleomagnetic results of Paleocene volcanic rocks from the Lhasa block: Tectonic implications for the collision of India and Asia. *Tectonophysics*, *490*(3–4), 257–266. <https://doi.org/10.1016/j.tecto.2010.05.011>
- Tong, Y., Yang, Z., Zheng, L., Yang, T., Shi, L., Sun, Z., & Pei, J. (2008). Early Paleocene paleomagnetic results from Southern Tibet, and tectonic implications. *International Geology Review*, *50*(6), 546–562. <https://doi.org/10.2747/0020-6814.50.6.546>
- Wang, Y., Meng, J., Beard, C., Li, Q., Ni, X., Gebo, D. L., et al. (2010). Early Paleogene stratigraphic sequences, mammalian evolution and its response to environmental changes in Erlian Basin, Inner Mongolia, China. *Science China Earth Sciences*, *53*(12), 1918–1926. <https://doi.org/10.1007/s11430-010-4095-8>
- Weltje, G. J. (1997). End-member modeling of compositional data: Numerical-statistical algorithms for solving the explicit mixing problem. *Mathematical Geology*, *29*(4), 503–549. <https://doi.org/10.1007/BF02775085>
- Xue, K., Ji, J., Zhang, K., Kou, X., Song, B., & Wang, C. (2013). Magnetostratigraphy and anisotropy of magnetic susceptibility of the Lulehe formation in the Northeastern Qaidam Basin. *Acta Geologica Sinica - English Edition*, *87*(2), 576–587. <https://doi.org/10.1111/1755-6724.12069>
- Ye, D. Q. (1993). In *Tertiary in petroliferous regions of China* (pp. 1–407). Petroleum Industry Press.
- Yin, A., & Harrison, T. M. (2000). Geologic evolution of the Himalayan-Tibetan orogen. *Annual Review of Earth and Planetary Sciences*, *28*(1), 211–280. <https://doi.org/10.1146/annurev.earth.28.1.211>
- Zhang, Y., Sun, D., Li, Z., Wang, F., Wang, X., Li, B., et al. (2014). Cenozoic record of aeolian sediment accumulation and aridification from Lanzhou, China, driven by Tibetan Plateau uplift and global climate. *Global and Planetary Change*, *120*, 1–15. <https://doi.org/10.1016/j.gloplacha.2014.05.009>
- Zheng, J. J., et al. (1999). *China stratigraphic code. Tertiary*. Geologic Press.

- Zhou, S., Mo, X., Dong, G., Zhao, Z., Qiu, R., Guo, T., & Wang, L. (2004). ^{40}Ar - ^{39}Ar geochronology of Cenozoic Linzizong volcanic rocks from Linzhou Basin, Tibet, China, and their geological implications. *Chinese Science Bulletin*, 49(18), 1970–1979. <https://doi.org/10.1360/03wd0511>
- Zhou, X., Jiang, Z., Quaye, J., Duan, Y., Hu, C., Liu, C., & Han, C. (2019). Ichnology and sedimentology of the trace fossil-bearing fluvial red beds from the lowermost member of the Paleocene Funing Formation in the Jinhu Depression, Subei Basin, East China. *Marine and Petroleum Geology*, 99, 393–415. <https://doi.org/10.1016/j.marpetgeo.2018.10.032>

References From the Supporting Information

- Biscaye, P. E. (1965). Mineralogy and sedimentation of recent deep-sea clay in the Atlantic Ocean and adjacent seas and oceans. *The Geological Society of America Bulletin*, 76(7), 803–832. [https://doi.org/10.1130/0016-7606\(1965\)76<803:MASORD>2.0.CO;2](https://doi.org/10.1130/0016-7606(1965)76<803:MASORD>2.0.CO;2)
- Chen, J., Li, G. J., Yang, J. D., Rao, W. B., Lu, H. Y., Balsam, W., et al. (2007). Nd and Sr isotopic characteristics of Chinese deserts: Implications for the provenances of Asian dust. *Geochimica et Cosmochimica Acta*, 71(15), 3904–3914. <https://doi.org/10.1016/j.gca.2007.04.033>
- Gallet, S., Jahn, B. M., & Torii, M. (1996). Geochemical characterization of the Luochuan loess-paleosol sequence, China, and paleoclimatic implications. *Chemical Geology*, 133(1–4), 67–88. [https://doi.org/10.1016/S0009-2541\(96\)00070-8](https://doi.org/10.1016/S0009-2541(96)00070-8)
- Gallet, S., Jahn, B. M., Lanoe, B. V., Dia, A., & Rossello, E. (1998). Loess geochemistry and its implications for particle origin and composition of the upper continental crust. *Earth and Planetary Science Letters*, 156(3–4), 157–172. [https://doi.org/10.1016/S0012-821X\(97\)00218-5](https://doi.org/10.1016/S0012-821X(97)00218-5)
- Goldstein, S. L., O’Nions, R. K., & Hamilton, P. J. (1984). A Sm-Nd isotopic study of atmospheric dusts and particulates from major river systems. *Earth and Planetary Science Letters*, 70(2), 221–236. [https://doi.org/10.1016/0012-821X\(84\)90007-4](https://doi.org/10.1016/0012-821X(84)90007-4)
- Hacker, B. R., Wang, X., Eide, E. A., & Ratschbacher, L. (1996). The Qinling-Dabie ultra-high-pressure collisional orogeny. In A. Yin, & T. M. Harrison (Eds.), *The tectonic evolution of Asia* (pp. 345–370). Cambridge University Press.
- Ke, X., Ji, J. L., Zhang, K. X., Kou, X. H., Song, B. W., & Wang, C. W. (2013). Magnetostratigraphy and anisotropy of magnetic susceptibility of the Lulehe Formation in the northeastern Qaidam Basin. *Acta Geologica Sinica*, 87(2), 576–587.
- Liu, J. S., Xu, H. Z., Jiang, Y. M., Wang, J., & He, X. J. (2020). Mesozoic and Cenozoic basin structure and tectonic evolution in the East China Sea basin. *Acta Geologica Sinica*, 94(3), 675–691.
- McFadden, P. L., & McElhinny, M. W. (1990). Classification of the reversal test in palaeomagnetism. *Geophysical Journal International*, 103(3), 725–729. <https://doi.org/10.1111/j.1365-246X.1990.tb05683.x>
- McLennan, S. M. (1989). Rare earth element in sedimentary rocks: Influence of provenance and sedimentary process. *Reviews in Mineralogy*, 21(1), 169–200. Retrieved from <https://pubs.geoscienceworld.org/msa/rimg/article/21/1/169/87254>
- Nesbitt, H. W., & Young, G. M. (1982). Early Proterozoic climates and plate motions inferred from major element chemistry of lutites. *Nature*, 299, 715–717. Retrieved from <https://www.nature.com/articles/299715a0>
- Pease, P. P., & Tchakerian, V. P. (2002). Composition and sources of sand in the Wahiba Sand Sea, Sultanate of Oman. *Annals of the Association of American Geographers*, 92(3), 416–434. <https://doi.org/10.1111/1467-8306.00297>
- Révilleon, S., Jouet, G., Bayon, G., Rabineau, M., Dennielou, B., Hémond, C., & Berné, S. (2011). The provenance of sediments in the Gulf of Lions, western Mediterranean Sea. *Geochemistry, Geophysics, Geosystems*, 12, Q08006. <https://doi.org/10.1029/2011GC003523>
- Singer, A. (1984). The paleoclimatic interpretation of clay minerals in sediments—A review. *Earth-Science Reviews*, 21(4), 251–293. [https://doi.org/10.1016/0012-8252\(84\)90055-2](https://doi.org/10.1016/0012-8252(84)90055-2)
- Wan, S., Yu, Z., Clift, P. D., Sun, H., Li, A., & Li, T. (2012). History of Asian eolian input to the West Philippine Sea over the last one million years. *Palaeogeography, Palaeoclimatology, Palaeoecology*, 326–328, 152–159. <https://doi.org/10.1016/j.palaeo.2012.02.015>
- Wang, M., & Shen, Z. K. (2020). Present-day crustal deformation of continental China derived from GPS and its tectonic implications. *Journal of Geophysical Research: Solid Earth*, 125, e2019JB018774. <https://doi.org/10.1029/2019JB018774>
- Xu, X. W., & Deng, Q. D. (1996). Nonlinear characteristics of paleoseismicity in China. *Journal of Geophysical Research*, 101(B3), 6209–6231. <https://doi.org/10.1029/95JB01238>
- Yang, C. S., Yang, C. Q., Shang, L. N., Yan, Z. H., & Yang, Y. Q. (2019). Discovery of Late Cretaceous–Paleocene faulted basins developed on the Yandang Low Uplift, East China Sea Shelf Basin. *China Geology*, 2, 243–244.
- Zdanowicz, C., Hall, G., Vaive, J., Amelin, Y., Percival, J., Girard, I., et al. (2006). Asian dustfall in the St. Elias Mountains, Yukon, Canada. *Geochimica et Cosmochimica Acta*, 70(14), 3493–3507. <https://doi.org/10.1016/j.gca.2006.05.005>
- Zhang, G. W., Guo, A. L., Wang, Y. J., Li, S. Z., Dong, Y. P., Liu, S. F., et al. (2013). Tectonics of South China continent and its implications. *Science China Earth Sciences*, 56(11), 1804–1828. <https://doi.org/10.1007/s11430-013-4679-1>
- Zhang, H. Y., Lu, H. Y., Jiang, S.-Y., Vandenberghe, J., Wang, S. J., & Cosgrove, R. (2012). Provenance of loess deposits in the Eastern Qinling Mountains (central China) and their implications for the paleoenvironment. *Quaternary Science Reviews*, 43, 94–102. <https://doi.org/10.1016/j.quascirev.2012.04.010>
- Zhang, P. Z., & Gan, W. J. (2008). Combined model of rigid-block motion with continuous deformation: Patterns of present-day deformation in continental China. In B. C. Burchfiel, & E. Wang (Eds.), *Investigations into the tectonics of the Tibetan Plateau: GSA spec.Pap.* (Vol. 444, pp. 59–71). [https://doi.org/10.1130/2008.2444\(04](https://doi.org/10.1130/2008.2444(04)